



University of HUDDERSFIELD

University of Huddersfield Repository

Montenegro, P.A., Neves, S.G.M., Calcada, R., Tanabe, M. and Sogabe, M.

Wheel–rail contact formulation for analyzing the lateral train–structure dynamic interaction

Original Citation

Montenegro, P.A., Neves, S.G.M., Calcada, R., Tanabe, M. and Sogabe, M. (2015) Wheel–rail contact formulation for analyzing the lateral train–structure dynamic interaction. *Computers & Structures*, 152. pp. 200-214. ISSN 0045-7949

This version is available at <http://eprints.hud.ac.uk/24588/>

The University Repository is a digital collection of the research output of the University, available on Open Access. Copyright and Moral Rights for the items on this site are retained by the individual author and/or other copyright owners. Users may access full items free of charge; copies of full text items generally can be reproduced, displayed or performed and given to third parties in any format or medium for personal research or study, educational or not-for-profit purposes without prior permission or charge, provided:

- The authors, title and full bibliographic details is credited in any copy;
- A hyperlink and/or URL is included for the original metadata page; and
- The content is not changed in any way.

For more information, including our policy and submission procedure, please contact the Repository Team at: E.mailbox@hud.ac.uk.

<http://eprints.hud.ac.uk/>

Wheel-rail contact formulation for analyzing the lateral train-structure dynamic interaction

P.A. Montenegro^{a,*}, S.G.M. Neves^a, R. Calçada^a, M. Tanabe^b, M. Sogabe^c

^a FEUP, Faculty of Engineering of the University of Porto, Rua Dr. Roberto Frias s/n, 4200-465 Porto, Portugal

^b KAIT, Kanagawa Institute of Technology, 1030 Shimo-ogino, Atsugi-shi, 243-0292, Kanagawa, Japan

^c RTRI, Railway Technical Research Institute, 2-8-38 Hikari-cho, Kokubunji-shi, 185-8540, Tokyo, Japan

ABSTRACT

A wheel-rail contact formulation for analyzing the train-structure nonlinear interaction that takes into account the wheel and rail geometry is proposed. Most of the existing methods treat the contact forces as external forces, whereas the present formulation uses a finite element to model the behavior in the contact interface, based on Hertz's theory and Kalker's laws. The equations of motion are complemented with constraint equations that relate the displacements of the vehicle and structure, being the complete system solved directly using an optimized algorithm. The formulation is validated with experimental data from a test performed on a rolling stock plant.

Keywords: Wheel-rail interaction, Geometric contact problem, Lateral dynamics, Experimental validation

1 Introduction

In more recent years, as train operating speeds increase, the dynamic effects caused by trains passing over bridges, the running safety and riding comfort of the train have become important issues in railway engineering. The design of high-speed railway bridges may be governed by limit states of the train, such as the running safety, rather than by limit states of the bridge. Therefore, the development of software capable of accurately and efficiently assessing the vehicle-structure lateral interaction became essential for structural and mechanical engineers. Taking into account the geometry of the wheel and rail surfaces in the analysis of the lateral

effects is particularly important for an accurate evaluation of the vehicle-structure interaction. Since this can significantly increase the computational cost, the algorithm used for analyzing the coupling of the two systems and the associated geometric contact problem is a key point of the methodology.

Several approaches to study the wheel-rail contact behavior can be found in the literature. A simple methodology consists of imposing the hunting motion of the wheelset as a harmonic prescribed displacement with amplitude and wavelength given by the Klingel formula [1-2]. Wu et al [3] proposed a new contact element based on a condensation technique that is used to impose the constraint equations between the vehicle and structure in the vertical and lateral directions. However, the relative motion between the wheel and rail and the corresponding tangential forces, which are essential for adequately model the lateral dynamics, are neglected by these methods.

Linear approaches [4] can be derived from the assumption of a constant conicity of the wheel profile. However, for scenarios such as strong lateral winds or earthquakes, the impacts between the wheel flange and the rail strongly influence the dynamic behavior, making the aforementioned models restricted to the analysis of the vehicle-structure interaction under normal operating conditions. To overcome this limitation, the geometries of the wheel and rail profiles have to be taken into account and a fully nonlinear formulation has to be used. In wheel-rail contact problems, since the normal and tangential forces significantly depend on the geometric characteristics of the surfaces near the contact point, the accuracy used for defining these surfaces is crucial.

The location of the contact points can be calculated using two different approaches. In the first approach, called offline contact search [5-7], an analysis of the geometry of the surfaces is previously performed, being the location of the contact points precalculated as a function of the

relative lateral displacement between the vehicle and structure and stored in a lookup table to be later interpolated during the dynamic analysis. This approach is computationally attractive but does not account for the penetration between the wheel and rail, which may have a significant influence. This limitation is overcome in the second approach, called online contact search [8-11], in which a set of nonlinear equations is solved in each step of the dynamic analysis to determine the exact position of the contact point. The higher accuracy obtained with this approach outweighs the additional computational cost.

An extension of the formulation described in [12-13] that takes into account the lateral dynamic effects between railway vehicles and structures is proposed in the present article. Most of the existing methods treat the contact forces in the normal and tangential directions as external forces, whereas the proposed formulation uses a finite element to model the behavior in the contact interface. This formulation is divided into three main parts: 1) the geometric problem consisting of the detection of the contact points; 2) the normal contact problem in which the forces are determined based on the Hertz nonlinear theory; 3) the tangential contact problem in which the creep forces, that appear due to the rolling friction contact, are calculated. The proposed method is based on the finite element method, which allows the analysis of structures and vehicles with any degree of complexity and the consideration of the deformations undergone by the two systems. The present formulation is implemented in MATLAB [14]. The vehicle and structure are modeled using ANSYS [15], being their structural matrices imported by MATLAB.

An experimental test performed in the rolling stock test plant of the Railway Technical Research Institute (RTRI) in Japan is used to validate the present method. This test consists of a railway vehicle mounted over four wheel-shaped rails that can be controlled independently in order to simulate different types of rail deviations. The results obtained with the proposed

formulation are compared with the experimental results, and also with the results obtained using the software DIASTARS developed by Tanabe et al. [7].

2 Wheel-rail contact elements

2.1 Enhanced contact element

In the majority of the currently available methods for analyzing the vehicle-structure interaction, the normal and tangential contact forces are treated as external forces. However, it is generally more efficient to use a finite element formulation based on the contact laws for the normal and tangential directions. A node-to-segment contact element that takes into account the behavior in the contact interface is proposed in the present article (see Fig. 1).

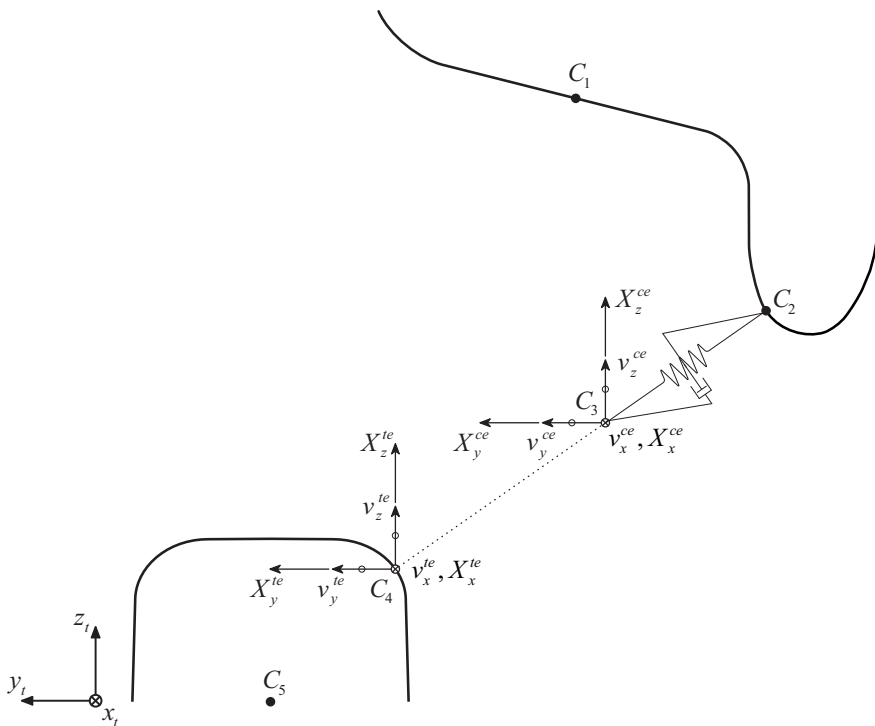


Fig. 1. Target and node-to-segment contact elements.

Figure 1 shows the forces \mathbf{X} acting at the contact interface and the displacements of the contact point \mathbf{v} , which are defined in the local coordinate system of the target element (x_t, y_t, z_t) .

The superscripts ce and te indicate contact and target element, respectively. The x_t axis has the direction of the longitudinal axis of the target element, the y_t axis is parallel to the track plane and the z_t axis completes the right-handed system. The node C_1 is a nodal point of the vehicle and the pilot point of the rigid surface of the wheel. The point C_5 is an auxiliary internal point of a target element of the structure and the pilot point of the rigid surface of the rail. The motions of the rigid surfaces of the wheel and rail are governed by the degrees of freedom of the corresponding pilot node. The auxiliary points C_2 and C_4 belong to the rigid surfaces of the wheel and rail, respectively. When contact occurs, the proposed enhanced node-to-segment contact element adds the internal node C_3 and the finite element connecting the point C_2 and the node C_3 in order to take into account the contact behavior in the normal and tangential directions.

When contact occurs, the node C_3 and the auxiliary point C_4 are coincident. The constraint equations that relate the displacements of these nodes are imposed using the direct method[13], which is extended to deal with three-dimensional contact problems. Since in the proposed contact element there are no moments transmitted across the contact interface, the constraint equations only relate the translational displacements in the three directions. This approach is acceptable, since the creep spin moments as well as the moments caused by the lateral slip are small in comparison with other moments acting on the system [16]. The relative motions between the wheel and rail are accounted by the finite element connecting the point C_2 and the node C_3 . The irregularities present at the contact interface can be considered in the constraint equations for the vertical and lateral directions.

Since the auxiliary points C_4 and C_5 do not belong to the mesh of the structure, the constraint equations that relate the displacements of the auxiliary point C_4 and the node C_3 , and the forces applied at the point C_4 have to be transformed in order to be associated with the degrees of freedom of the nodes of the target element. A similar transformation has to be applied to the

finite element connecting the point C_2 and the node C_3 in order to be associated with the degrees of freedom of the node C_1 .

2.2 Contact behavior in the normal and tangential directions

The stiffness and damping matrices of the contact element depicted in Fig. 1 are first calculated in the contact point coordinate system (x_c, y_c, z_c) illustrated in Fig. 2 and then transformed to the global coordinate system. This local coordinate system follows the motion of the contact point, being its origin attached to the center of the contact area.

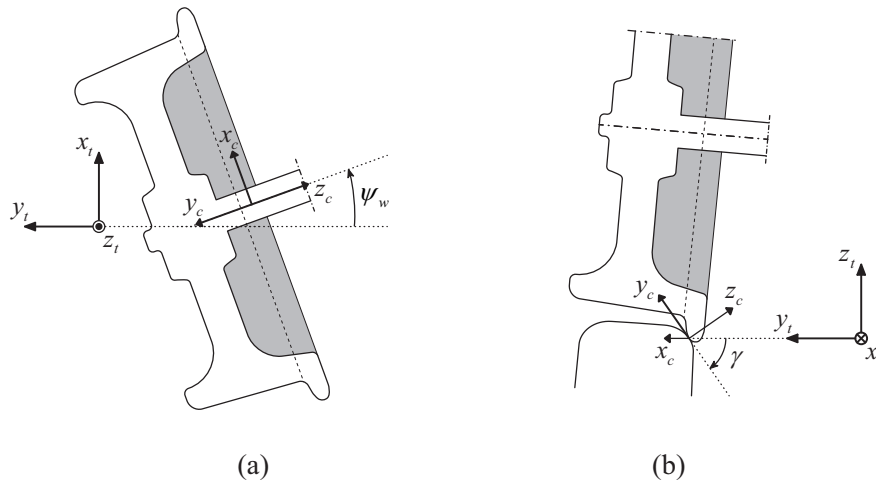


Fig. 2. Contact point coordinate system: (a) top view and (b) front view.

The z_c axis is oriented along the direction normal to the contact plane, the x_c axis points towards the longitudinal direction of motion and the y_c axis completes the right-handed system. The normal forces are defined along the z_c axis, and the longitudinal and lateral tangential forces are defined along the x_c and y_c axes, respectively. The yaw and contact angles are denoted by ψ_w and γ , respectively.

The transformation matrix \mathbf{T}^{gc} from the global coordinate system to the contact point coordinate system is given by

$$\mathbf{T}^{gc} = \mathbf{T}_x^{tc} \mathbf{T}_z^{tc} \mathbf{T}^{gt} \quad (1)$$

where

$$\mathbf{T}_z^{tc} = \begin{bmatrix} \cos \psi_w & \sin \psi_w & 0 \\ -\sin \psi_w & \cos \psi_w & 0 \\ 0 & 0 & 1 \end{bmatrix} \quad (2)$$

$$\mathbf{T}_x^{tc} = \begin{bmatrix} 1 & 0 & 0 \\ 0 & \cos \gamma & \sin \gamma \\ 0 & -\sin \gamma & \cos \gamma \end{bmatrix} \quad (3)$$

The matrices \mathbf{T}_z^{tc} and \mathbf{T}_x^{tc} transform from the target element coordinate system to the contact point coordinate system, and correspond to a rotation of ψ_w about the z_t axis and a rotation of γ about the x_t , respectively. The matrix \mathbf{T}^{gt} represents the standard transformation from the global coordinate system to the local coordinate system of the target element [17].

The analysis of the behavior in the contact interface is divided into two main problems: 1) the normal contact problem, which results from the compression between the wheel and rail; 2) the tangential contact problem, which is a consequence of the local elasticity of the contacting surfaces, and of the rolling friction phenomenon that characterizes the contact between two bodies that roll over each other. Assuming that the bodies in contact have the same material properties, the normal and tangential problems can be solved separately.

When two non-conforming bodies are loaded they will deform in the vicinity of the point of first contact, touching over an area. The normal contact problem is analyzed based on the nonlinear Hertz contact theory [18]. This theory can only deal with non-conformal contact where the contact area is small when compared with the dimensions of the two bodies and with the relative radii of curvature of the surfaces. However, this assumption is acceptable in railway applications, since the wheel and rail have considerably different shapes. In the present article an

elliptical contact area is assumed. The normal contact force F_n between the wheel and rail is given by

$$F_n = K_h d^{\frac{3}{2}} \quad (4)$$

where d is the penetration and K_h is a generalized stiffness coefficient that depends on the material properties of the bodies in contact, such as the Young modulus and the Poisson ratio, and on the curvatures of the surfaces at the contact point [19-20]. Since the Hertz law is given by a closed-form expression, the tangent stiffness matrix \mathbf{K} can be updated at each iteration in order to take advantage of the full Newton-Raphson method [21].

If two bodies that are compressed against each other are allowed to roll over each other, some points on the contact area may slip while others may adhere. The difference between the tangential strains of the bodies in the adhesion area leads to a small apparent slip, called creep. The creep, which depends on the relative velocities of the two bodies at the contact point, is crucial for the determination of the tangential forces that develop in the contact area, called creep forces. These forces can be calculated through three dimensionless parameters, called creepages, defined with respect to the contact point coordinate system (see Fig. 2). These are the longitudinal creepage, the lateral creepage and the spin creepage.

The longitudinal creepage v_ξ and the lateral creepage v_η are the relative velocities between the wheel and rail at the contact point along the x_c and y_c axes, respectively, normalized to the vehicle forward velocity V , given by

$$v_\xi = \frac{(\dot{\mathbf{a}}_w - \dot{\mathbf{a}}_r) \cdot \mathbf{e}_{x_c}}{V} \quad (5)$$

$$v_\eta = \frac{(\dot{\mathbf{a}}_w - \dot{\mathbf{a}}_r) \cdot \mathbf{e}_{y_c}}{V} \quad (6)$$

where $\dot{\mathbf{a}}_w$ and $\dot{\mathbf{a}}_r$ are the vectors of translational velocities of the wheel and rail at the contact point, respectively, defined with respect to the global coordinate system, and \mathbf{e}_{x_c} and \mathbf{e}_{y_c} are unit base vectors of the contact point coordinate system.

The spin creepage V_ϕ is the relative angular velocity between the wheel and rail at the contact point about the z_c axis normalized to the vehicle forward velocity, given by

$$V_\phi = \frac{(\dot{\boldsymbol{\omega}}_w - \dot{\boldsymbol{\omega}}_r) \cdot \mathbf{e}_{z_c}}{V} \quad (7)$$

in which $\dot{\boldsymbol{\omega}}_w$ and $\dot{\boldsymbol{\omega}}_r$ are the vectors of rotational velocities of the wheel and rail at the contact point, respectively, defined with respect to the global coordinate system, and \mathbf{e}_{z_c} is a unit base vector of the contact point coordinate system.

In the present work, the longitudinal creep force F_ξ and the lateral creep force F_η are precalculated and stored in a lookup table, based on USETAB [22], to be later interpolated during the dynamic analysis as a function of the creepages and the semi-axes ratio of the contact ellipse. As mentioned in Section 2.1, the creep moments are neglected in the present work. This table has been calculated with the software CONTACT [23] which is based on Kalker's exact three-dimensional rolling contact theory [24]. The lookup table uses an effective layout, exploiting all possible symmetries between the contact forces and creepages [25]. The values of the table are normalized and calculated according to the procedure described in [22].

For constructing the table, the normalized creepages and semi-axes ratios have been discretized in two intervals as in the original USETAB, namely $0 \leq x \leq 1$ and $1 \leq x < \infty$, where x is the input of the table. A linear and a logarithmic distribution of ten values were used for the discretization of the first and second intervals, respectively. Adopting a 40×40 element discretization of the contact ellipse, and by considering all possible combinations of the

creepages and semi-axes ratios, a total of 320000 calculations have been performed using the software CONTACT.

Since the contact law based on the exact theory of rolling contact proposed by Kalker cannot be expressed with a closed-form expression, calculating the numerical derivatives with respect to the nodal velocities can be computationally expensive. Therefore, the initial tangent damping matrix \mathbf{C} is calculated based on the Kalker's linear theory [25] and is kept constant throughout the analysis.

The nodal forces \mathbf{R}^c corresponding to the internal element stresses, the tangent stiffness matrix \mathbf{K}^c and the tangent damping matrix \mathbf{C}^c are transformed from the local point coordinate system to the global coordinate system, according to

$$\mathbf{R} = \mathbf{T}^{gcT} \mathbf{R}^c \quad (8)$$

$$\mathbf{K} = \mathbf{T}^{gcT} \mathbf{K}^c \mathbf{T}^{gc} \quad (9)$$

$$\mathbf{C} = \mathbf{T}^{gcT} \mathbf{C}^c \mathbf{T}^{gc} \quad (10)$$

where \mathbf{T}^{gc} is the transformation matrix defined by Eq. (1). The superscript c indicates that the quantity is defined with respect to the contact point coordinate system.

3 Parameterization of the rail and wheel profiles

The location of the contact points, which depends on the correct representation of the wheel and rail surfaces, is a key point to obtain an accurate solution of the contact problem. In the present formulation, the profile surfaces are parameterized as a function of surface parameters using piecewise cubic interpolation. The parameterization of each surface is performed using cubic splines, defined from a set of control points that are representative of the profile geometry.

In situations where the yaw rotation plays an important role, such as curve negotiations or railway turnouts, the wheel may contact the rail in two points located at different diametric sections, namely at the tread and the flange. In these circumstances, the flange contact point can be located ahead or behind the tread contact point, giving origin to lead or lag contact configurations, respectively [9]. Since only straight track scenarios are analyzed, this type of analysis is beyond the scope of the present work, restricting the contact point search to only one plane. Therefore, the geometrical parameterization is formulated in terms of two surface parameters s_r and s_w that define the lateral location of the contact point in the rail and wheel, respectively, with respect to their local coordinate systems.

3.1 Coordinate systems of the rail and wheel profiles

The rail profile coordinate system (x_r, y_r, z_r) is fixed with the rail and has its origin at the point where the wheel contacts the rail when the wheelset is centered with the track. The y_r and z_r axes belong to the rail cross section plane, being the former oriented along the tangent to the surface at the contact point. The transformation from the target element coordinate system to the rail profile coordinate system is given by

$$\mathbf{T}^r = \begin{bmatrix} 1 & 0 & 0 \\ 0 & \cos \phi_r & \sin \phi_r \\ 0 & -\sin \phi_r & \cos \phi_r \end{bmatrix} \quad (11)$$

where ϕ_r is the roll rotation of the rail about the target element longitudinal axis x_t .

The wheel profile coordinate system (x_w, y_w, z_w) has the same origin of the rail profile coordinate system, being the orientation defined by the roll rotation of the wheel about the x_t axis. Since the contact point search is restricted to only one plane, the yaw angle contribution is

neglected in the geometrical problem [5, 7-8]. Thus, the transformation from the target element coordinate system to the wheel profile coordinate system can be written as

$$\mathbf{T}^{rw} = \begin{bmatrix} 1 & 0 & 0 \\ 0 & \cos \phi_w & \sin \phi_w \\ 0 & -\sin \phi_w & \cos \phi_w \end{bmatrix} \quad (12)$$

where ϕ_w is the roll rotation of the wheel about the target element longitudinal axis x_t .

3.2 Parameterization of the rail profile

The two-dimensional surface geometry of the rail is described in terms of the surface parameter s_r , as depicted in Fig. 3.

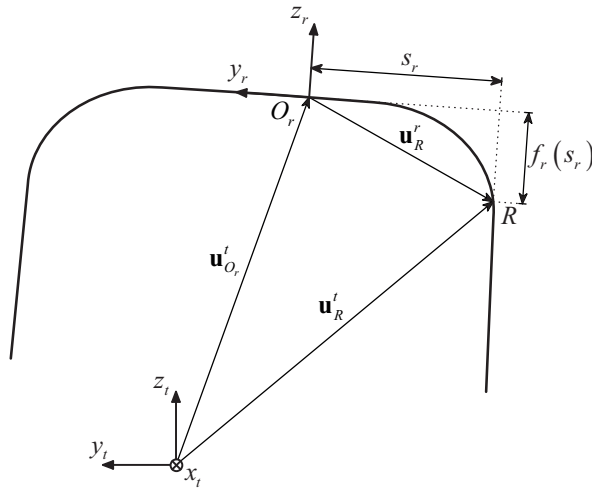


Fig. 3. Parameterization of the rail profile.

The position vector \mathbf{u}_R^t of an arbitrary point R of the rail surface, defined with respect to the target element coordinate system, is given by

$$\mathbf{u}_R^t = \mathbf{u}_{O_r}^t + \mathbf{T}^{rwT} \mathbf{u}_R^r \quad (13)$$

where \mathbf{u}'_O is the position vector of the origin of the rail profile coordinate system, defined with respect to the target element coordinate system, and \mathbf{u}^r_R is the position vector of the arbitrary point of the rail surface defined in the rail profile coordinate system, written as

$$\mathbf{u}^r_R = [0 \quad s_r \quad f_r(s_r)]^T \quad (14)$$

in which $f_r(s_r)$ is the function defining the rail surface.

In the implemented wheel-rail contact formulation, the normal and tangent vectors to the rail surface at the contact point are necessary to calculate its location. The tangent vector to the rail surface at the contact point along the lateral direction $\mathbf{t}^t_{r,y}$ defined with respect to the target element coordinate system is given by

$$\mathbf{t}^t_{r,y} = \mathbf{T}^{trT} \mathbf{t}^r_{r,y} \quad (15)$$

where the tangent vector $\mathbf{t}^r_{r,y}$, defined with respect to the rail profile coordinate system, is obtained by differentiating the rail surface function with respect to the surface parameter, i.e.,

$$\mathbf{t}^r_{r,y} = \left[0 \quad 1 \quad \frac{df_r(s_r)}{ds_r} \right]^T \quad (16)$$

Since the location of the contact point is determined through a planar geometric analysis, the tangent vector along the longitudinal direction $\mathbf{t}^t_{r,x}$ has the same direction as the x_t axis. The normal vector to the rail surface \mathbf{n}^t_r at the contact point defined with respect to the target element coordinate system is given by

$$\mathbf{n}^t_r = \mathbf{t}^t_{r,x} \times \mathbf{t}^t_{r,y} \quad (17)$$

with \mathbf{n}^t_r pointing outwards the surface.

Finally, the contact angle γ , defined between the lateral tangent vector and the track plane, is given by

$$\gamma = \tan^{-1}\left(\frac{df_r(s_r)}{ds_r}\right) + \phi_r \quad (18)$$

Note that the roll rotation ϕ_r is the angle between the rail profile coordinate system and the target element coordinate system.

3.3 Parameterization of the wheel profile

The method proposed in the present paper allows the detection of two contact points between the wheel and rail. To this end, the wheel is parameterized by two functions, one for the tread and another for the flange, making the location of the contact points in each region of the wheel fully independent.

Figure 4 shows the parameterization of the wheel profile in terms of a single surface parameter s_w to clarify the illustration. However, each of the aforementioned functions that define the wheel surface is defined by an independent surface parameter.

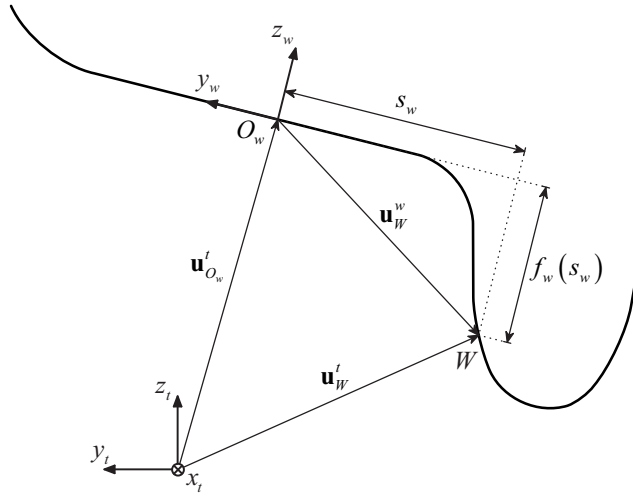


Fig. 4. Parameterization of the wheel profile.

The position vector \mathbf{u}_W^t of an arbitrary point W of the wheel surface, defined with respect to the target element coordinate system, is given by

$$\mathbf{u}_W^t = \mathbf{u}_{O_w}^t + \mathbf{T}^{tw^T} \mathbf{u}_W^w \quad (19)$$

in which $\mathbf{u}_{O_w}^t$ is the position vector of the origin of the wheel profile coordinate system, defined with respect to the target element coordinate system, and \mathbf{u}_W^w is the position vector of the arbitrary point of the wheel surface defined in the wheel profile coordinate system, written as

$$\mathbf{u}_W^w = [0 \quad s_w \quad f_w(s_w)]^T \quad (20)$$

where $f_w(s_w)$ is the function defining the tread or flange surfaces.

The tangent and normal vectors to the wheel surface at the contact point, $\mathbf{t}_{w,y}^t$ and \mathbf{n}_w^t , defined with respect to the target element coordinate system, are calculated in an analogous way as in Section 3.2.

4 Geometric contact problem

To determine the location of the potential contact points between the wheel and rail, the following set of nonlinear equations is used.

$$\begin{cases} \mathbf{t}_{r,y}^t \cdot \mathbf{d}_{wr}^t = 0 \\ \mathbf{t}_{w,y}^t \cdot \mathbf{n}_r^t = 0 \end{cases} \quad (21)$$

where $\mathbf{t}_{r,y}^t$, $\mathbf{t}_{w,y}^t$ and \mathbf{n}_r^t are defined in Section 3 and \mathbf{d}_{wr}^t is the vector that defines the relative position of the point of the wheel with respect to the point of the rail, given by

$$\mathbf{d}_{wr}^t = \mathbf{u}_W^t - \mathbf{u}_R^t \quad (22)$$

where \mathbf{u}_W^t and \mathbf{u}_R^t are given by Eqs. (19) and (13). The first condition described by Eq. (21) ensures that the tangent vector to the rail is perpendicular to the vector defining the relative position of the point of the wheel with respect to the point of the rail. The second condition ensures that the normal vector to the rail is perpendicular to the tangent vector to the wheel, as depicted in Fig. 5.

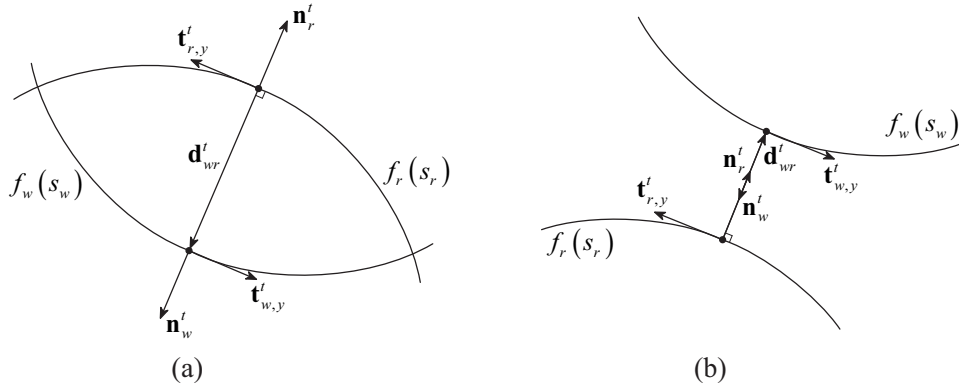


Fig. 5. Potential contact points between the two surfaces: (a) actual contact and (b) no contact.

It is important to notice that the system of equations (21) may have multiple solutions if one of the contact surfaces is not convex. Therefore, the concave region in the transition zone between the tread and flange is neglected, and an approximation to the surface is adopted [9].

In the present formulation, an internal function of MATLAB is used to solve the nonlinear algebraic equations (21). This function uses an iterative scheme based on the Newton method together with a trust-region technique to improve the robustness of the algorithm and handle situations where the Jacobian matrix of the algebraic equations is singular [14].

The potential contact points determined with the procedure described above have to fulfill a last condition, that is, the parametric surfaces have to intersect each other. As shown in Fig. 5b, the conditions described in Eq. (21) are satisfied but there is no contact. This condition can be expressed mathematically as

$$\mathbf{d}_{wr}^t \cdot \mathbf{n}_r^t \leq 0 \quad (23)$$

which means that the intersection between two bodies is guaranteed only if the vectors \mathbf{d}_{wr}^t and \mathbf{n}_r^t point in opposite directions, as shown in Fig. 5a. The penetration d between the two bodies in contact is given by

$$d = \|\mathbf{d}_{wr}^t\| \quad (24)$$

Since the contact point detection is a nonlinear problem, an initial estimate for the solution has to be given to solve the iterative process. In most cases, in order to reduce the number of iterations, the solution obtained in the previous iteration/step is used as an initial guess to solve the current iteration. However, if flange contact occurs, the contact point position suffers an abrupt jump from the tread to the flange and the previous obtained solution may not be an appropriate estimation for the current iteration. This can cause the solution to converge very slow or even diverge. Therefore, an accurate prediction of jumps in the contact point position leads to a faster solution and eliminates some of the causes responsible for convergence problems during the contact solver.

The contact point jump detection proposed in this paper consists of precalculating a lookup table, similar to those used in the offline multibody formulations [5-7]. These lookup tables follow the assumption of a rigid contact between wheel and rail, in which the surface parameters that define the contact point position can be computed as a function of the relative lateral displacement between the center of mass of the wheelset and the track centerline. Thereafter, the proposed table can predict if there is a contact point in the flange for a given relative lateral displacement. Since the proposed methodology is based on the finite element method instead of a multibody formulation, this table is only used to estimate if there is flange contact. If so, the surface parameters obtained by table interpolation are used as an initial guess to detect the potential new flange contact point. Thus, when solving the nonlinear algebraic equations (21), a higher convergence rate is achieved due to a more accurate initial estimate. The procedure for implementing the contact lookup table is described in Appendix B.

5 Formulation of the vehicle-structure interaction problem

Neves et al. [13] developed an accurate and efficient algorithm, referred to as the direct method, in which the governing equilibrium equations of the vehicle and structure are complemented with additional constraint equations that relate the displacements of the contact nodes of the vehicle with the corresponding nodal displacements of the structure. These equations form a single system, with displacements and contact forces as unknowns, that is solved directly using an optimized block factorization algorithm.

5.1 Governing equations of motion

Considering the α method [26], the equations of motion of the vehicle-structure system can be written as

$$\mathbf{M} \ddot{\mathbf{a}}^{t+\Delta t} + (1+\alpha) \mathbf{R}^{t+\Delta t} - \alpha \mathbf{R}^t = (1+\alpha) \mathbf{F}^{t+\Delta t} - \alpha \mathbf{F}^t \quad (25)$$

where \mathbf{M} is the mass matrix, \mathbf{R} are the nodal forces corresponding to the internal element stresses, \mathbf{F} are the externally applied nodal loads and \mathbf{a} are the nodal displacements. The elastic and damping forces depend nonlinearly on the nodal displacements and velocities due to the nonlinear nature of contact. In the present work, the nonlinear inertia effects, such as the centrifugal and gyroscopic effects, are neglected. The superscripts t and $t + \Delta t$ indicate the previous and current time step, respectively.

To solve Eq. (25) let the F type degrees of freedom (d.o.f.) represent the free nodal d.o.f., whose values are unknown, and let the P type d.o.f. represent the prescribed nodal d.o.f., whose values are known. Thus, the load vector can be expressed as

$$\mathbf{F}_F = \mathbf{P}_F + \mathbf{D}_{FX}^{ce} \mathbf{X}^{ce} + \mathbf{D}_{FX}^{te} \mathbf{X}^{te} \quad (26)$$

$$\mathbf{F}_P = \mathbf{P}_P + \mathbf{D}_{PX}^{te} \mathbf{X}^{te} + \mathbf{S} \quad (27)$$

where \mathbf{P} corresponds to the externally applied nodal loads whose values are known, \mathbf{S} are the support reactions and \mathbf{X} are the forces acting at the contact interface shown in Fig. 1. Each matrix \mathbf{D} relates the contact forces, defined with respect to the target element coordinate system, with the nodal forces defined in the global coordinate system.

According to Newton's third law, the forces acting at the contact interface must be of equal magnitude and opposite direction (see Fig. 1), i.e.,

$$\mathbf{X}^{ce} + \mathbf{X}^{te} = \mathbf{0} \quad (28)$$

Substituting Eq. (28) into Eqs. (26) and (27) leads to

$$\mathbf{F}_F = \mathbf{P}_F + \mathbf{D}_{FX} \mathbf{X} \quad (29)$$

$$\mathbf{F}_P = \mathbf{P}_P + \mathbf{D}_{PX} \mathbf{X} + \mathbf{S} \quad (30)$$

where

$$\mathbf{X} = \mathbf{X}^{ce} \quad (31)$$

$$\mathbf{D}_{FX} = \mathbf{D}_{FX}^{ce} - \mathbf{D}_{FX}^{te} \quad (32)$$

$$\mathbf{D}_{PX} = -\mathbf{D}_{PX}^{te} \quad (33)$$

Substituting Eqs. (29) and (30) into Eq. (25), and partitioning into F and P type d.o.f., gives

$$\begin{aligned} & \begin{bmatrix} \mathbf{M}_{FF} & \mathbf{M}_{FP} \\ \mathbf{M}_{PF} & \mathbf{M}_{PP} \end{bmatrix} \begin{bmatrix} \ddot{\mathbf{a}}_F^{t+\Delta t} \\ \ddot{\mathbf{a}}_P^{t+\Delta t} \end{bmatrix} + (1+\alpha) \begin{bmatrix} \mathbf{R}_F^{t+\Delta t} \\ \mathbf{R}_P^{t+\Delta t} \end{bmatrix} - \alpha \begin{bmatrix} \mathbf{R}_F^t \\ \mathbf{R}_P^t \end{bmatrix} \\ & = (1+\alpha) \begin{bmatrix} \mathbf{P}_F^{t+\Delta t} + \mathbf{D}_{FX}^{t+\Delta t} \mathbf{X}^{t+\Delta t} \\ \mathbf{P}_P^{t+\Delta t} + \mathbf{D}_{PX}^{t+\Delta t} \mathbf{X}^{t+\Delta t} + \mathbf{S}^{t+\Delta t} \end{bmatrix} - \alpha \begin{bmatrix} \mathbf{P}_F^t + \mathbf{D}_{FX}^t \mathbf{X}^t \\ \mathbf{P}_P^t + \mathbf{D}_{PX}^t \mathbf{X}^t + \mathbf{S}^t \end{bmatrix} \end{aligned} \quad (34)$$

Considering only the first row of Eq. (34) and transferring the unknowns to the left-hand side leads to

$$\mathbf{M}_{FF} \ddot{\mathbf{a}}_F^{t+\Delta t} + (1+\alpha) \mathbf{R}_F^{t+\Delta t} - (1+\alpha) \mathbf{D}_{FX}^{t+\Delta t} \mathbf{X}^{t+\Delta t} = \bar{\mathbf{F}}_F \quad (35)$$

where

$$\bar{\mathbf{F}}_F = (1+\alpha) \mathbf{P}_F^{t+\Delta t} - \alpha \mathbf{P}_F^t - \alpha \mathbf{D}_{FX}^t \mathbf{X}^t - \mathbf{M}_{FP} \ddot{\mathbf{a}}_P^{t+\Delta t} + \alpha \mathbf{R}_F^t \quad (36)$$

Since the present problem has a nonlinear nature, Eq. (35) is rewritten in the form

$$\boldsymbol{\Psi}_F(\mathbf{a}_F^{t+\Delta t}, \mathbf{X}^{t+\Delta t}) = \mathbf{0} \quad (37)$$

where $\boldsymbol{\Psi}_F$ is the residual force vector, given by

$$\boldsymbol{\Psi}_F(\mathbf{a}_F^{t+\Delta t}, \mathbf{X}^{t+\Delta t}) = \bar{\mathbf{F}}_F - \mathbf{M}_{FF} \ddot{\mathbf{a}}_F^{t+\Delta t} - (1+\alpha)\mathbf{R}_F^{t+\Delta t} + (1+\alpha)\mathbf{D}_{FX}^{t+\Delta t} \mathbf{X}^{t+\Delta t} \quad (38)$$

The nodal velocities and accelerations depend on the nodal displacements and for this reason are not independent unknowns. According to the α method, the following approximations for the acceleration and velocity at the current time step can be obtained [13].

$$\ddot{a}^{t+\Delta t} = \frac{1}{\beta\Delta t^2}(a^{t+\Delta t} - a^t) - \frac{1}{\beta\Delta t}\dot{a}^t - \left(\frac{1}{2\beta} - 1\right)\ddot{a}^t \quad (39)$$

$$\dot{a}^{t+\Delta t} = \frac{\gamma}{\beta\Delta t}(a^{t+\Delta t} - a^t) + \left(1 - \frac{\gamma}{\beta}\right)\dot{a}^t + \Delta t \left(1 - \frac{\gamma}{2\beta}\right)\ddot{a}^t \quad (40)$$

where β and γ are parameters that control the stability and accuracy of the method.

An iterative scheme based on the Newton method [21] is used to solve Eq. (37). Assuming that the solution at the i th Newton iteration has been evaluated and neglecting second and higher order terms, the Taylor series for $\boldsymbol{\Psi}_F$ about $(\mathbf{a}_F^{t+\Delta t, i}, \mathbf{X}^{t+\Delta t, i})$ is given by

$$\begin{aligned} \boldsymbol{\Psi}_F(\mathbf{a}_F^{t+\Delta t, i+1}, \mathbf{X}^{t+\Delta t, i+1}) &= \boldsymbol{\Psi}_F(\mathbf{a}_F^{t+\Delta t, i}, \mathbf{X}^{t+\Delta t, i}) + \left[\frac{\partial \boldsymbol{\Psi}_F}{\partial \mathbf{a}_F^{t+\Delta t}} \bigg|_{(\mathbf{a}_F^{t+\Delta t, i}, \mathbf{X}^{t+\Delta t, i})} \right] (\mathbf{a}_F^{t+\Delta t, i+1} - \mathbf{a}_F^{t+\Delta t, i}) \\ &\quad + \left[\frac{\partial \boldsymbol{\Psi}_F}{\partial \mathbf{X}^{t+\Delta t}} \bigg|_{(\mathbf{a}_F^{t+\Delta t, i}, \mathbf{X}^{t+\Delta t, i})} \right] (\mathbf{X}^{t+\Delta t, i+1} - \mathbf{X}^{t+\Delta t, i}) \end{aligned} \quad (41)$$

Substituting Eqs. (38) to (40) into Eq. (41), and assuming that the residual force vector at iteration $i+1$ fulfils the condition given by Eq. (37), leads to

$$\begin{aligned} \boldsymbol{\Psi}_F(\mathbf{a}_F^{t+\Delta t, i}, \mathbf{X}^{t+\Delta t, i}) &+ \left[-\frac{1}{\beta\Delta t^2} \mathbf{M}_{FF} - (1+\alpha) \left[\frac{\partial \mathbf{R}_F}{\partial \mathbf{a}_F^{t+\Delta t}} \bigg|_{\mathbf{a}_F^{t+\Delta t, i}} \right] \right] (\mathbf{a}_F^{t+\Delta t, i+1} - \mathbf{a}_F^{t+\Delta t, i}) \\ &+ (1+\alpha)\mathbf{D}_{FX}^{t+\Delta t, i} (\mathbf{X}^{t+\Delta t, i+1} - \mathbf{X}^{t+\Delta t, i}) = \mathbf{0} \end{aligned} \quad (42)$$

Transforming Eq. (42) into an incremental form leads to

$$\bar{\mathbf{K}}_{FF} \Delta \mathbf{a}_F^{i+1} - (1 + \alpha) \mathbf{D}_{FX}^{t+\Delta t, i} \Delta \mathbf{X}^{i+1} = \boldsymbol{\Psi}_F^i \quad (43)$$

where $\bar{\mathbf{K}}_{FF}$ is the current effective stiffness matrix defined by

$$\bar{\mathbf{K}}_{FF} = \frac{1}{\beta \Delta t^2} \mathbf{M}_{FF} + (1 + \alpha) \left[\frac{\partial \mathbf{R}_F}{\partial \mathbf{a}_F^{t+\Delta t}} \bigg|_{\mathbf{a}_F^{t+\Delta t, i}} \right] \quad (44)$$

and

$$\Delta \mathbf{a}_F^{i+1} = \mathbf{a}_F^{t+\Delta t, i+1} - \mathbf{a}_F^{t+\Delta t, i} \quad (45)$$

$$\Delta \mathbf{X}^{i+1} = \mathbf{X}^{t+\Delta t, i+1} - \mathbf{X}^{t+\Delta t, i} \quad (46)$$

$$\boldsymbol{\Psi}_F^i = \boldsymbol{\Psi}_F(\mathbf{a}_F^{t+\Delta t, i}, \mathbf{X}^{t+\Delta t, i}) \quad (47)$$

In matrix notation, Eq. (43) can be expressed as

$$\begin{bmatrix} \bar{\mathbf{K}}_{FF} & \bar{\mathbf{D}}_{FX} \end{bmatrix} \begin{bmatrix} \Delta \mathbf{a}_F^{i+1} \\ \Delta \mathbf{X}^{i+1} \end{bmatrix} = \boldsymbol{\Psi}_F^i \quad (48)$$

being

$$\bar{\mathbf{D}}_{FX} = -(1 + \alpha) \mathbf{D}_{FX}^{t+\Delta t, i} \quad (49)$$

After evaluating the solution at iteration $i+1$, the residual force vector is calculated using Eq. (38). The iteration scheme continues until the condition

$$\frac{\|\boldsymbol{\Psi}_F^{i+1}\|}{\|\mathbf{P}_F^{t+\Delta t}\|} \leq \varepsilon \quad (50)$$

is fulfilled, where ε is a specified tolerance.

5.2 Contact constraint equations

When contact occurs, the additional internal node of the contact element and the auxiliary point belonging to the rigid surface of the target element are coupled in the three directions (see Section 2.1). Thus, the following constraint equations must be imposed:

$$\mathbf{v}^{ce} - \mathbf{v}^{te} = \mathbf{r} \quad (51)$$

where \mathbf{r} are the irregularities between the contact and target elements in the vertical and lateral directions. The displacements of the additional internal nodes (see Fig. 1) are given by

$$\mathbf{v}^{ce} = \mathbf{H}_{XF}^{ce} \mathbf{a}_F^{t+\Delta t, i+1} \quad (52)$$

where the transformation matrix \mathbf{H} relates the displacements of the additional internal nodes of the contact element, defined in the global coordinate system, with the displacements defined in the local coordinate system of the corresponding target element. The displacements of the auxiliary points of the target elements are given by

$$\mathbf{v}^{te} = \mathbf{H}_{XF}^{te} \mathbf{a}_F^{t+\Delta t, i+1} + \mathbf{H}_{XP}^{te} \mathbf{a}_P^{t+\Delta t} \quad (53)$$

where each transformation matrix \mathbf{H} relates the nodal displacements of the target elements, defined in the global coordinate system, with the displacements of the auxiliary points defined in the target element coordinate system.

Substituting Eqs. (52) and (53) into Eq. (51) yields

$$\mathbf{H}_{XF} \mathbf{a}_F^{t+\Delta t, i+1} = \mathbf{r} - \mathbf{H}_{XP} \mathbf{a}_P^{t+\Delta t} \quad (54)$$

where

$$\mathbf{H}_{XF} = \mathbf{H}_{XF}^{ce} - \mathbf{H}_{XF}^{te} \quad (55)$$

$$\mathbf{H}_{XP} = -\mathbf{H}_{XP}^{te} \quad (56)$$

Rearranging Eq. (54) in terms of $\mathbf{a}_F^{t+\Delta t, i+1}$ and substituting into Eq. (54) leads to

$$\mathbf{H}_{XF} \Delta \mathbf{a}_F^{i+1} = \mathbf{r} - \mathbf{H}_{XP} \mathbf{a}_P^{t+\Delta t} - \mathbf{H}_{XF} \mathbf{a}_F^{t+\Delta t, i} \quad (57)$$

Multiplying Eq. (57) by $-(1+\alpha)$ gives

$$\bar{\mathbf{H}}_{XF} \Delta \mathbf{a}_F^{i+1} = \bar{\mathbf{r}} \quad (58)$$

where

$$\bar{\mathbf{H}}_{XF} = -(1+\alpha) \mathbf{H}_{XF} \quad (59)$$

and

$$\bar{\mathbf{r}} = -(1 + \alpha) \left(\mathbf{r} - \mathbf{H}_{XP} \mathbf{a}_P^{t+\Delta t} - \mathbf{H}_{XF} \mathbf{a}_F^{t+\Delta t, i} \right) \quad (60)$$

5.3 Complete system of equations

The incremental formulation of the governing equations of motion of the vehicle-structure system is applicable to either linear or nonlinear analyses. These equations and the contact constraints form a complete system whose unknowns are incremental nodal displacements and incremental contact forces. Equations (48) and (58) can be expressed in matrix form leading to the following system of equations

$$\begin{bmatrix} \bar{\mathbf{K}}_{FF} & \bar{\mathbf{D}}_{FX} \\ \bar{\mathbf{H}}_{XF} & \mathbf{0} \end{bmatrix} \begin{bmatrix} \Delta \mathbf{a}_F^{i+1} \\ \Delta \mathbf{X}^{i+1} \end{bmatrix} = \begin{bmatrix} \boldsymbol{\Psi}_F^i \\ \bar{\mathbf{r}} \end{bmatrix} \quad (61)$$

Using Betti's theorem, it can be demonstrated that the matrix in Eq. (61) is symmetric. The corresponding proof is not presented here due to space limitations. Since the time required to solve the system of linear equations presented in Eq. (61) may represent a significant percentage of the total solution time, the efficiency of the solver is very important. The system matrix is partitioned into the following form in order to improve the efficiency of the solver.

$$\begin{bmatrix} \bar{\mathbf{K}}_{II} & \bar{\mathbf{K}}_{IR} & \bar{\mathbf{K}}_{IY} & \bar{\mathbf{D}}_{IX} \\ \bar{\mathbf{K}}_{RI} & \bar{\mathbf{K}}_{RR} & \bar{\mathbf{K}}_{RY} & \bar{\mathbf{D}}_{RX} \\ \bar{\mathbf{K}}_{YI} & \bar{\mathbf{K}}_{YR} & \bar{\mathbf{K}}_{YY} & \bar{\mathbf{D}}_{YX} \\ \bar{\mathbf{H}}_{XI} & \bar{\mathbf{H}}_{XR} & \bar{\mathbf{H}}_{XY} & \mathbf{0} \end{bmatrix} \begin{bmatrix} \Delta \mathbf{a}_I^{i+1} \\ \Delta \mathbf{a}_R^{i+1} \\ \Delta \mathbf{a}_Y^{i+1} \\ \Delta \mathbf{X}^{i+1} \end{bmatrix} = \begin{bmatrix} \boldsymbol{\Psi}_I^i \\ \boldsymbol{\Psi}_R^i \\ \boldsymbol{\Psi}_Y^i \\ \bar{\mathbf{r}} \end{bmatrix} \quad (62)$$

The F type d.o.f. are partitioned into I , R and Y type d.o.f. The Y type d.o.f. correspond to the d.o.f of the internal nodes added by the contact elements (see node C_3 in Fig. 1). These d.o.f. have to be grouped together because they are only active when contact occurs, and so the size of the matrices relating these d.o.f. is time-dependent. Since the laws for the contact interface are nonlinear, the matrices of the contact elements are also time-dependent. The R type d.o.f. correspond to all the nodal d.o.f of the contact elements, except for the Y type d.o.f., which have

already been separately grouped together (see node C_1 in Fig. 1). The I type d.o.f. are all the remaining F type d.o.f. The R type d.o.f. can also include the d.o.f of other finite elements that have nonlinear behavior such as the spring-dampers modeling the suspensions of vehicles. The present method adopts an efficient block factorization algorithm (see Appendix A), based on the one developed by Neves et al. [12].

5.4 Algorithm for solving the vehicle-structure interaction problem

The proposed vehicle-structure interaction method has been implemented in MATLAB, being the vehicles and structures modeled with ANSYS. All the data regarding these models, such as the structural matrices, the definition of the target elements, the contact nodes of the vehicle and the support conditions are exported by ANSYS in batch mode and subsequently imported by MATLAB. The remaining data, namely the irregularities between the wheel and rail, the external applied loads, the contact lookup table and the control points defining the rail and wheel profile surfaces are stored in an external database and imported directly by MATLAB.

After all the data is imported and processed, an initial static analysis is performed in order to obtain the initial conditions of the dynamic problem. The flowchart depicted in Fig. 6 illustrates all the aspects regarding the dynamic analysis of the vehicle-structure interaction.

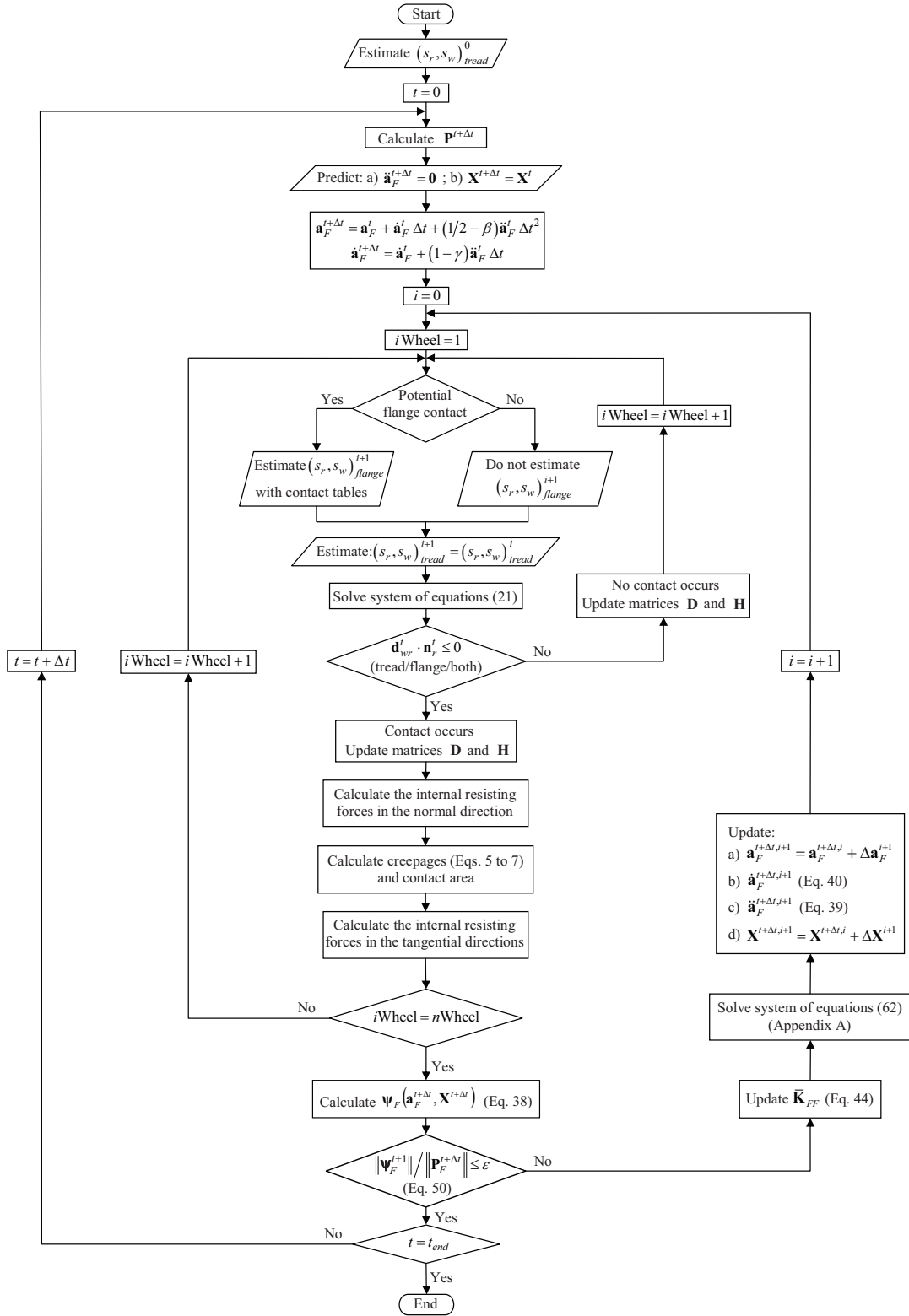


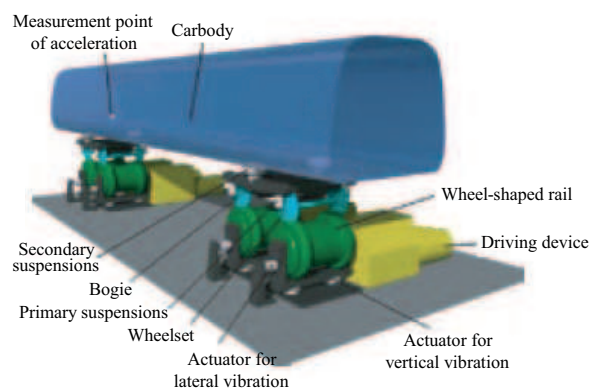
Fig. 6. Flowchart of the algorithm for analyzing the vehicle-structure dynamic interaction.

6 Application case

High-speed railway lines require a more rigorous maintenance when compared with conventional lines. Since the displacements of the structures may contribute to significant track deviations, and subsequently influence the riding comfort or the running safety of the train, deflection limits should be imposed during the design of railway structures. Such precautions are particularly important in countries prone to earthquakes, where large lateral displacements may occur during a seismic event. Japan, with one of the largest railway networks in the world, is one of those countries. Thus, the Committee on Displacement Limit of Structures Associated with the Runnability of Railway Vehicles, consisting of engineers and academics specialized in the design of railway structures and in the study of vehicle dynamics, proposed a displacement limit standard for railway structures based on numerical and experimental results [27]. One of the experimental tests, conducted in the rolling stock test plant in RTRI, consists in the analysis of a railway vehicle mounted over four wheel-shaped rails controlled by independent actuators that can simulate different types of rail deviations (see Fig. 7). A detailed discussion about the experimental test can be found in [28].



(a)



(b)

Fig. 7. Experimental test: (a) rolling stock test plant [29] and (b) test setup (adapted from [30]).

In the present application, the test mentioned above is simulated using the proposed method and the software DIASTARS developed by Tanabe et al. [31], being the results obtained compared with the experimental data.

The test vehicle consists on a narrow gauge prototype car specially developed for the experimental test. A schematic representation of the dynamic model of the test vehicle is illustrated in Fig. 8. The springs and dampers of the suspensions are denoted by k and c and the masses and rotary inertias are indicated by m and I . The longitudinal, lateral and vertical distances are denoted by a , b and h , respectively, s refers to the lateral distance between the initial contact points and R_0 is the nominal rolling radius. The subscripts cb , b and w indicate carbody, bogie and wheelset, respectively.

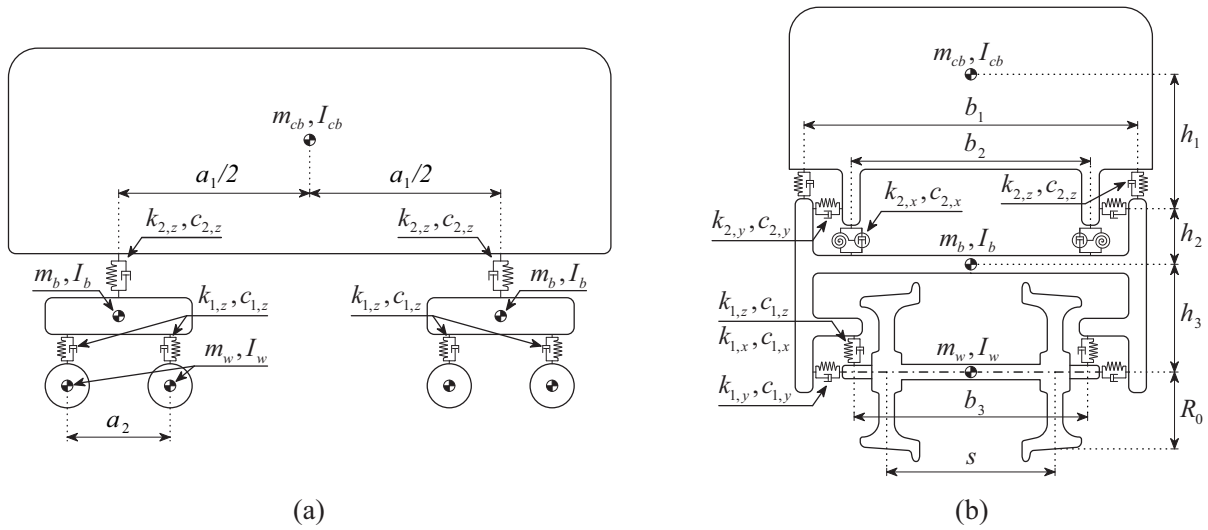


Fig. 8. Dynamic model of the test vehicle: (a) lateral view and (b) front view.

The carbody, bogies and wheelsets are modeled using beam finite elements, and the suspensions are modeled using spring-dampers in the three directions, as depicted in Fig. 9. The masses and rotary inertias are modeled using mass point elements, located at the center of mass of each component.

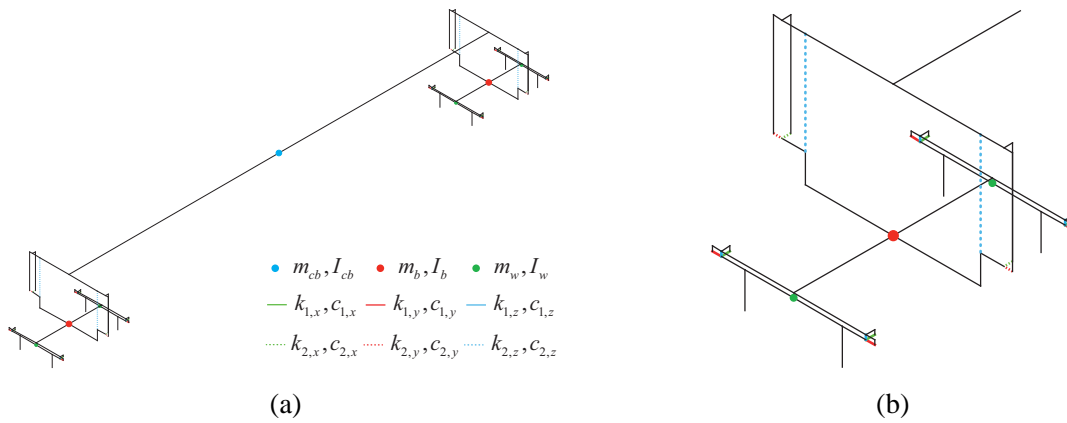


Fig. 9. Finite element model of the test vehicle: (a) full perspective and (b) detail of the bogie.

The numerical mode shapes and the corresponding frequencies of the test train presented in Fig. 10 were computed with ANSYS. The carbody and bogie are denoted by CB and BG, respectively.

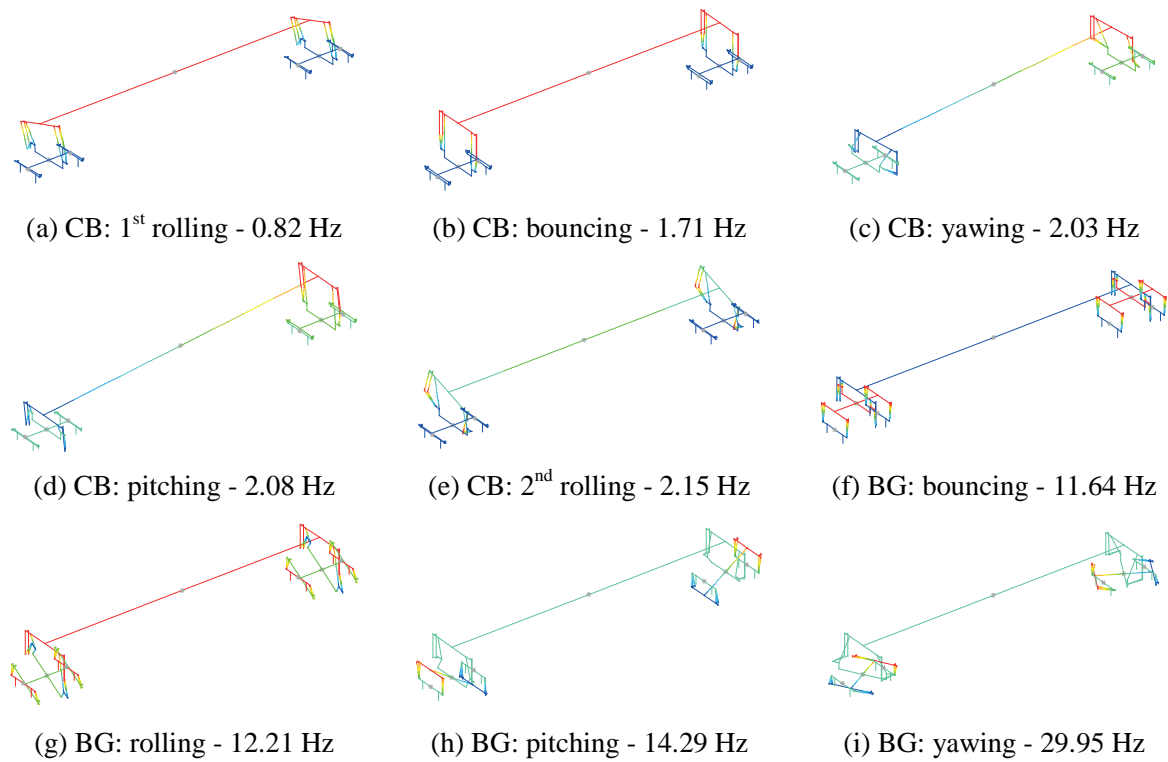


Fig. 10. Numerical frequencies and mode shapes of the railway vehicle.

The structure shown in Fig. 11 is modeled with rigid finite elements, being the track deviation included as an irregularity in the lateral direction. These deviations can occur due to the deflection of the bridge during a seismic event, thus causing high levels of vibrations in the train that can jeopardize the running safety. The deflection types considered in the present application are divided into two: a bending shape (BS), associated with the bending of two consecutive spans, and a translation shape (TS), in which only one span rotates while the other is subjected to a translation (see Fig. 11). In the present application, span lengths L of 20 m and 40 m are considered.

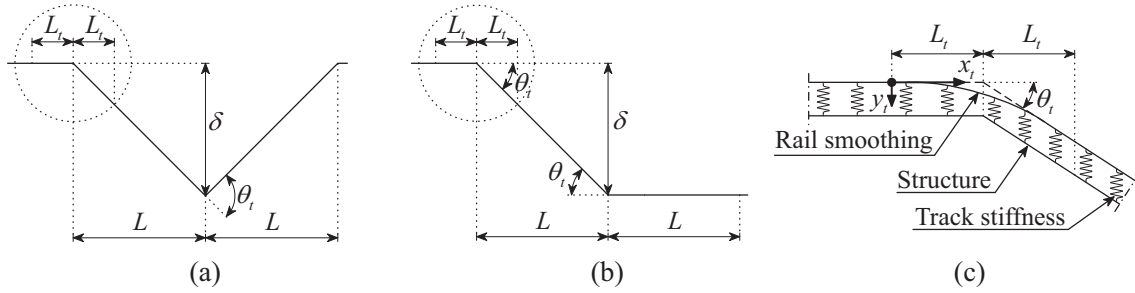


Fig. 11. Deflection models: (a) BS, (b) TS and (c) detail of the transition.

Transition sections have been included at both ends of each span due to the continuity of rotations of the rail (see Fig. 11c). The half length of the total transition zone is denoted by L_t , the span rotation by θ_i and the distance from the start of the transition zone by x_i . This procedure avoids numerical problems associated with unrealistic impacts that may occur if the transitions are abrupt. Hence, according to [28, 30], the track deviation y_i in the transition zone is given by

$$y_i = \begin{cases} \frac{\theta_i}{4\beta} e^{\beta(x_i - L_t)} \{ \cos [\beta(x_i - L_t)] + \sin [\beta(x_i - L_t)] \} & ; 0 \leq x_i \leq L_t \\ \frac{\theta_i}{4\beta} e^{-\beta(x_i - L_t)} \{ \cos [\beta(x_i - L_t)] + \sin [\beta(x_i - L_t)] \} + \theta_i(x_i - L_t) & ; L_t < x_i \leq 2L_t \end{cases} \quad (63)$$

where β is the relative bending stiffness of the rails and pads in the lateral direction, given by

$$\beta = \sqrt[4]{\frac{k_p}{4EI_r}} \quad (64)$$

where k_p is the pad stiffness, E the Young modulus of the steel and I_r the moment of inertia of the rail. The parameters used for defining the transition zones are summarized in Table 1.

Table 1
Parameters of the transition zones.

Variable	Value
L_t	3 m
k_p	4.8×10^5 kN/m/m
I_r	509 cm ⁴

The rail profile used in the numerical analysis is the JIS60 profile, while the wheel is a conic and arc profile wheel with diameter of 860 mm [32] same as that used in the Shinkansen trains (see Fig. 12). Since the geometric problem may have multiple solutions if one of the contact surfaces is concave, an approximation to the transition zone between the tread and flange is adopted.

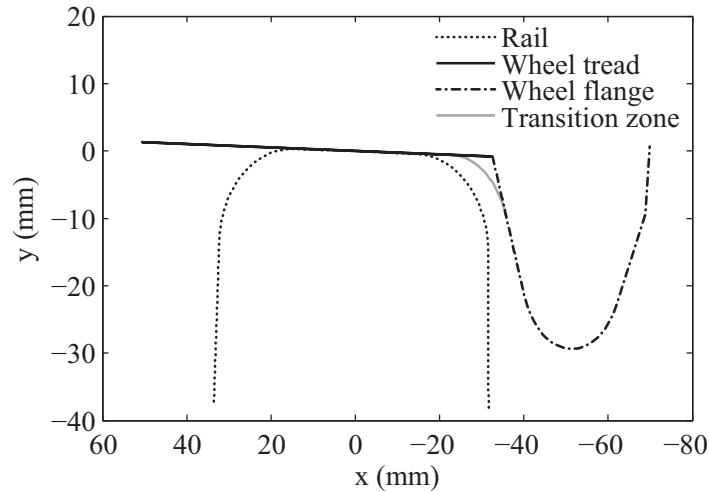


Fig. 12. Wheel and rail profiles used in simulation.

During the experimental test, the carbody lateral accelerations were measured above the rear bogie. The test was conducted with a railway vehicle riding over the test stand at 300 km/h and

subjected to lateral vibrations caused by the actuators. The maximum deflection amplitude considered in all scenarios is $\delta = 8$ mm (see Fig. 11).

The time step used in all the performed analysis is $\Delta t = 0.001$ s and the total number of time steps is 2500. Since DIASTARS uses the Newmark integration scheme to solve the equations of motion, no numerical dissipation is considered in the α method in order to establish a more reliable comparison. Therefore, the parameters $\alpha = 0$, $\beta = 0.25$ and $\gamma = 0.5$ are adopted.

The comparison between the lateral accelerations measured in the carbody above the rear bogie and the results obtained with the proposed method and DIASTARS is depicted in Fig. 13. A good agreement can be observed between the measured data and the numerical results. The differences observed may be justified by the fact that the numerical model of the vehicle does not consider the flexibility of some components, especially the carbody, where the accelerations were measured. The lack of additional experimental data to calibrate the vehicle model may also contribute to these differences. When comparing the numerical results obtained with the proposed method and with DIASTARS an excellent agreement can be observed. The slight differences may be due to the fact that the two numerical formulations are based on different wheel-rail contact models. The DIASTARS uses an offline contact search algorithm and a creep model based on Kalker's linear theory with a saturation limit for high creepages, whereas the proposed method uses an online contact search formulation and the USETAB tables to compute the creep forces.

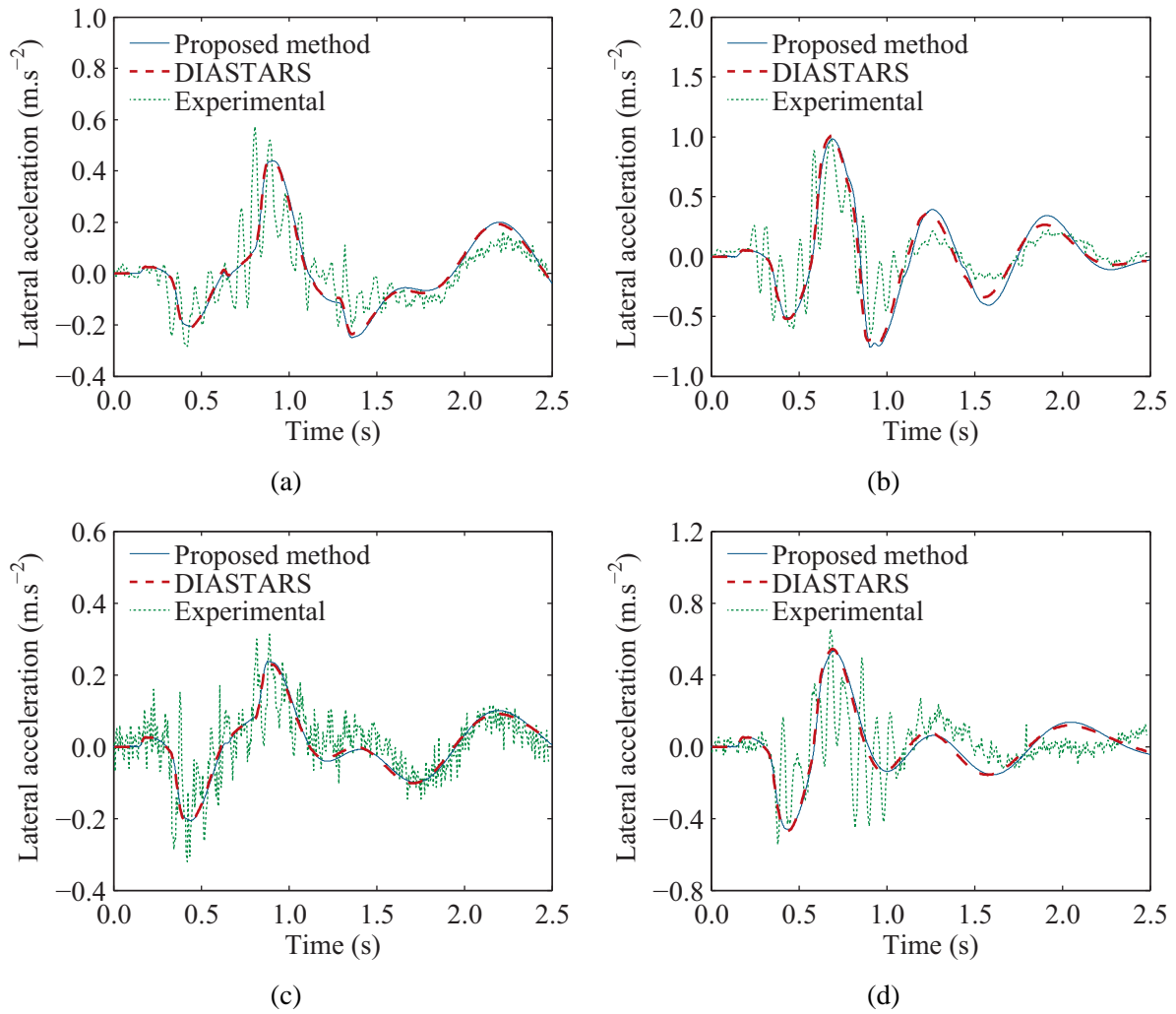


Fig. 13. Lateral accelerations in the carbody above the rear bogie: (a) BS - 40 m span; (b) BS - 20 m span; (c) TS - 40 m span; (d) TS - 20 m span.

As previously mentioned, the experimental data is restricted to the acceleration in the carbody above the rear bogie. Nevertheless, for a more accurate validation, the results obtained with the proposed method in other components of the railway vehicle are compared with those obtained with DIASTARS. Only results regarding the BS test with a 20 m span and the TS test with a 40 m span are presented hereafter due to space limitations.

The lateral displacements and accelerations at the center of mass of the first wheelset obtained in the BS and TS tests are plotted in Figs. 14 and 15, respectively.

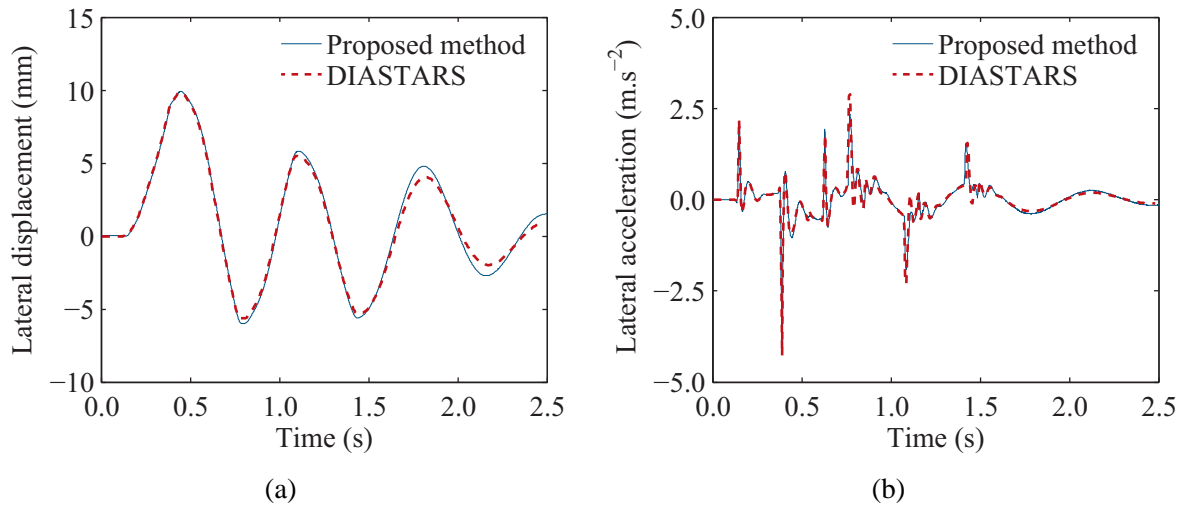


Fig. 14. Lateral response of the first wheelset obtained in the BS test: (a) displacements and (b) accelerations.

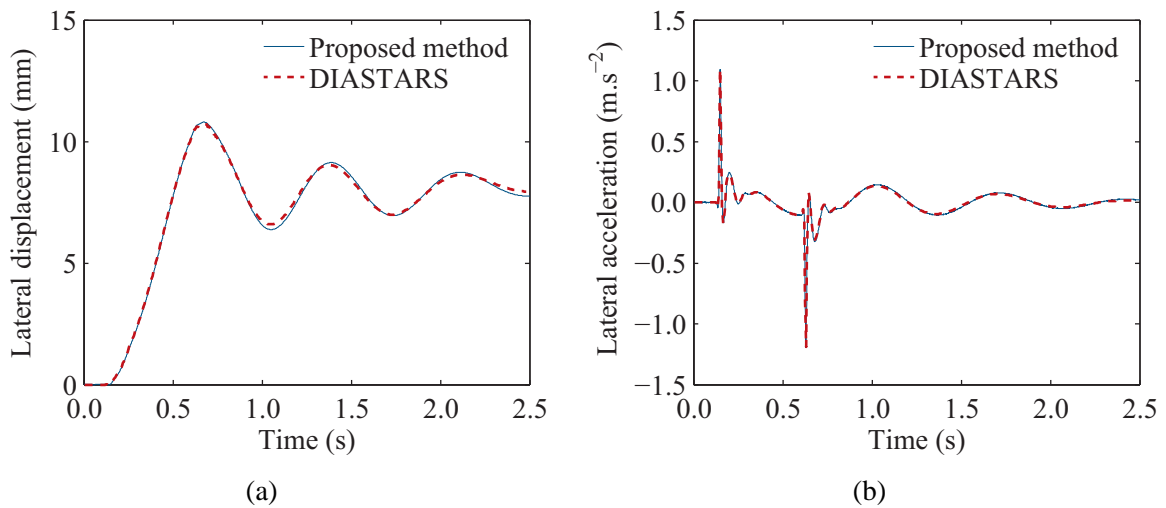


Fig. 15. Lateral response of the first wheelset obtained in the TS test: (a) displacements and (b) accelerations.

Finally, the contact forces in the wheels of the first wheelset for the BS and TS tests are plotted in Figs. 16 and 17, respectively. In the BS test, three flange impacts can be observed when the contact force suddenly increases: one in the left wheel, approximately at 1.1 s, and two in the right wheel, at 0.8 s and 1.4 s. The functions defining the BS and TS deflection models are the same for the first span (see Fig. 11). Therefore, the higher contact forces obtained in the BS

test, when the wheelset enters the first span, are due the fact that span deviation is more abrupt in the BS test, .i.e., the maximum deflection amplitude is the same in both tests but the span lengths are different. Again the results obtained with both numerical methods show an excellent agreement.

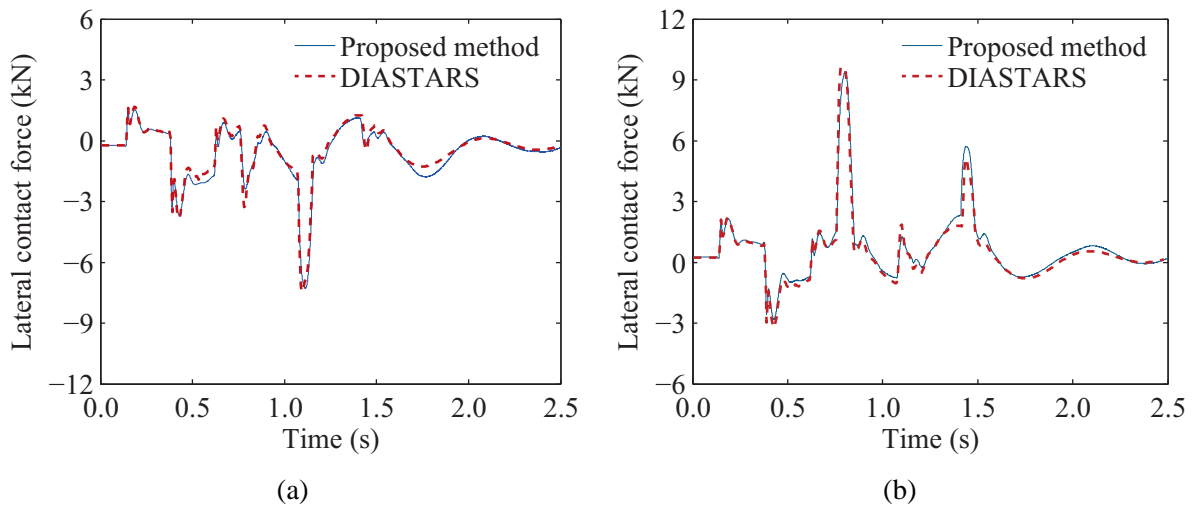


Fig. 16. Lateral contact force obtained in the BS test: (a) left wheel and (b) right wheel of the first wheelset.

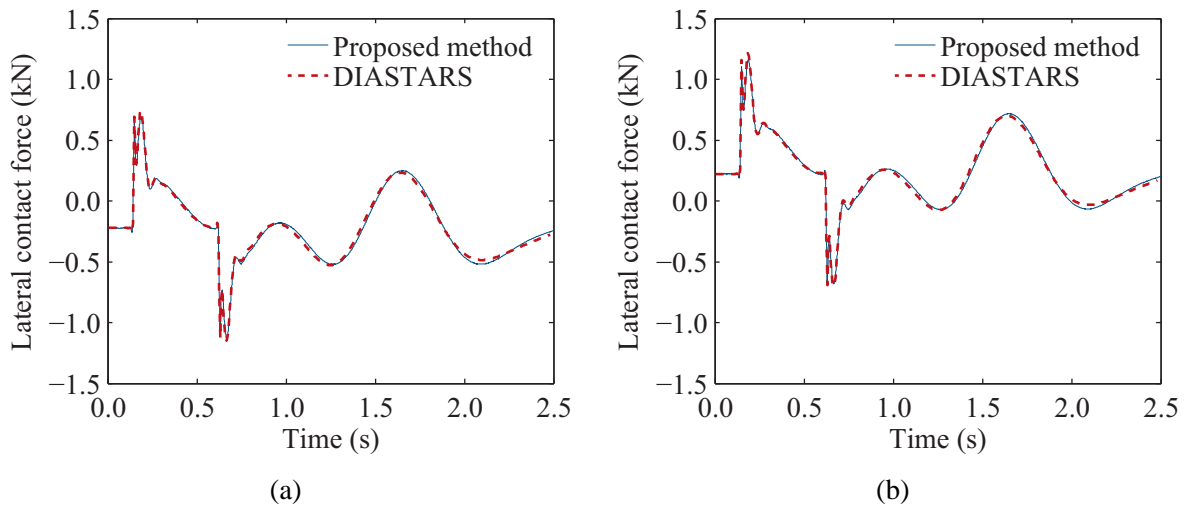


Fig. 17. Lateral contact force obtained in the TS test: (a) left wheel and (b) right wheel of the first wheelset.

7 Conclusions

A wheel-rail contact formulation for analyzing the nonlinear dynamic interaction between vehicles and structures is proposed in this article. This method takes into account the geometry of the wheel and rail surfaces in order to accurately evaluate the lateral interaction.

An enhanced node-to-segment contact element is used for modeling the behavior in the contact interface in the normal and tangential directions. This approach is generally more efficient than treating the normal and tangential contact forces as external forces. The constraint equations that relate the displacements of the vehicle and structure are imposed using a direct method. In contrast with other contact formulations such as the penalty method, the proposed formulation does not require additional penalty parameters and is less likely to lead to ill-conditioned systems.

The proposed formulation is validated using the results obtained in an experimental test performed in the rolling stock test plant of the Railway Technical Research Institute in Japan. This test consists of a full scale railway vehicle running over four wheel-shaped rails controlled by actuators that impose rail deviations in the lateral direction. The lateral accelerations inside the carbody have been measured and compared with those obtained with the proposed method and with DIASTARS. The results show a good agreement, especially when the two numerical methods are compared. Regarding the experimental results, the discrepancies observed may be caused by the fact that vehicle is modeled using rigid bars and thus important deformations were not considered.

An application of the proposed method regarding the evaluation of a real running safety scenario of a train crossing a bridge subjected to earthquakes will be presented in a forthcoming publication.

Acknowledgements

This article reports research developed under financial support provided by "FCT - Fundação para a Ciência e Tecnologia", Portugal, under grants SFRH/BD/48320/2008 and SFRH/BD/39190/2007.

Appendix A. Block factorization solver

Since the submatrix $\bar{\mathbf{K}}_{yy}$ presented in Eq. (62) may be indefinite and therefore may not have a stable factorization without pivoting, the lines and columns of the system matrix corresponding to the incremental displacements $\Delta \mathbf{a}_y$ and contact forces $\Delta \mathbf{X}$ have to be grouped together. Hence the block factorization of the system of equations (62) is presented below using the following notation.

$$\begin{bmatrix} \mathbf{A}_{11} & \mathbf{A}_{21}^T & \mathbf{A}_{31}^T \\ \mathbf{A}_{21} & \mathbf{A}_{22} & \mathbf{A}_{32}^T \\ \mathbf{A}_{31} & \mathbf{A}_{32} & \mathbf{A}_{33} \end{bmatrix} \begin{bmatrix} \mathbf{x}_1 \\ \mathbf{x}_2 \\ \mathbf{x}_3 \end{bmatrix} = \begin{bmatrix} \mathbf{b}_1 \\ \mathbf{b}_2 \\ \mathbf{b}_3 \end{bmatrix} \quad (\text{A.1})$$

where \mathbf{x}_1 and \mathbf{x}_2 correspond to $\Delta \mathbf{a}_l$ and $\Delta \mathbf{a}_r$, respectively, and \mathbf{x}_3 corresponds to the group formed by $\Delta \mathbf{a}_y$ and $\Delta \mathbf{X}$. The coefficient matrix presented in Eq. (A.1) admits the following factorization

$$\begin{bmatrix} \mathbf{A}_{11} & \mathbf{A}_{21}^T & \mathbf{A}_{31}^T \\ \mathbf{A}_{21} & \mathbf{A}_{22} & \mathbf{A}_{32}^T \\ \mathbf{A}_{31} & \mathbf{A}_{32} & \mathbf{A}_{33} \end{bmatrix} = \begin{bmatrix} \mathbf{L}_{11} & \mathbf{0} & \mathbf{0} \\ \mathbf{L}_{21} & \mathbf{L}_{22} & \mathbf{0} \\ \mathbf{L}_{31} & \mathbf{L}_{32} & \mathbf{L}_{33} \end{bmatrix} \times \begin{bmatrix} \mathbf{L}_{11}^T & \mathbf{L}_{21}^T & \mathbf{L}_{31}^T \\ \mathbf{0} & \mathbf{L}_{22}^T & \mathbf{L}_{32}^T \\ \mathbf{0} & \mathbf{0} & \mathbf{U}_{33} \end{bmatrix} \quad (\text{A.2})$$

where \mathbf{L} and \mathbf{U} are lower and upper triangular matrices, respectively. For simplicity, the permutation matrices associated with the factorization of \mathbf{A}_{33} are not represented. The block factorization solver is divided into three stages, which are described below.

By equating part of the corresponding blocks in Eq. (A.2) the following relations are obtained

$$\mathbf{A}_{11} = \mathbf{L}_{11} \mathbf{L}_{11}^T \quad (\text{A.3})$$

$$\mathbf{A}_{21}^T = \mathbf{L}_{11} \mathbf{L}_{21}^T \quad (\text{A.4})$$

The first stage consists of factorizing \mathbf{A}_{11} , which is assumed to be symmetric positive definite and therefore admits a Cholesky factorization [33], and calculating \mathbf{L}_{21} by forward substitution. Since \mathbf{A}_{11} and \mathbf{A}_{21}^T are time-independent, the operations associated with Eqs. (A.3) and (A.4) have to be performed only once at the beginning of the analysis.

By equating the remaining blocks in Eq. (A.2) the following relations are obtained

$$\mathbf{A}_{31}^T = \mathbf{L}_{11} \mathbf{L}_{31}^T \quad (\text{A.5})$$

$$\bar{\mathbf{A}}_{22} = \mathbf{L}_{22} \mathbf{L}_{22}^T \quad (\text{A.6})$$

$$\mathbf{A}_{32}^T = \mathbf{L}_{21} \mathbf{L}_{31}^T + \mathbf{L}_{22} \mathbf{L}_{32}^T \quad (\text{A.7})$$

$$\bar{\mathbf{A}}_{33} = \mathbf{L}_{33} \mathbf{U}_{33} \quad (\text{A.8})$$

where

$$\bar{\mathbf{A}}_{22} = \mathbf{A}_{22} - \mathbf{L}_{21} \mathbf{L}_{21}^T \quad (\text{A.9})$$

$$\bar{\mathbf{A}}_{33} = \mathbf{A}_{33} - \mathbf{L}_{31} \mathbf{L}_{31}^T - \mathbf{L}_{32} \mathbf{L}_{32}^T \quad (\text{A.10})$$

The second stage consists of obtaining the remaining matrices of the right hand side of Eq. (A.2) in an analogous way. It is assumed that the matrix $\bar{\mathbf{A}}_{22}$ admits a Cholesky factorization, whereas the submatrices \mathbf{L}_{33} and \mathbf{U}_{33} are obtained using an *LU* factorization with pivoting. Since the matrices involved in Eqs. (A.5) to (A.8) depend on the time and contact conditions, the operations belonging to the second stage have to be performed in each Newton iteration.

Finally, the third stage of the block factorization algorithm consists of obtaining the solution of the system of equations through the following two steps.

$$\begin{bmatrix} \mathbf{L}_{11} & \mathbf{0} & \mathbf{0} \\ \mathbf{L}_{21} & \mathbf{L}_{22} & \mathbf{0} \\ \mathbf{L}_{31} & \mathbf{L}_{32} & \mathbf{L}_{33} \end{bmatrix} \begin{bmatrix} \mathbf{y}_1 \\ \mathbf{y}_2 \\ \mathbf{y}_3 \end{bmatrix} = \begin{bmatrix} \mathbf{b}_1 \\ \mathbf{b}_2 \\ \mathbf{b}_3 \end{bmatrix} \quad (\text{A.11})$$

$$\begin{bmatrix} \mathbf{L}_{11}^T & \mathbf{L}_{21}^T & \mathbf{L}_{31}^T \\ \mathbf{0} & \mathbf{L}_{22}^T & \mathbf{L}_{32}^T \\ \mathbf{0} & \mathbf{0} & \mathbf{U}_{33} \end{bmatrix} \begin{bmatrix} \mathbf{x}_1 \\ \mathbf{x}_2 \\ \mathbf{x}_3 \end{bmatrix} = \begin{bmatrix} \mathbf{y}_1 \\ \mathbf{y}_2 \\ \mathbf{y}_3 \end{bmatrix} \quad (\text{A.12})$$

The vectors \mathbf{y}_1 to \mathbf{y}_3 are obtained by forward substitution as following

$$\mathbf{L}_{11} \mathbf{y}_1 = \mathbf{b}_1 \quad (\text{A.13})$$

$$\mathbf{L}_{22} \mathbf{y}_2 = \mathbf{b}_2 - \mathbf{L}_{21} \mathbf{y}_1 \quad (\text{A.14})$$

$$\mathbf{L}_{33} \mathbf{y}_3 = \mathbf{b}_3 - \mathbf{L}_{31} \mathbf{y}_1 - \mathbf{L}_{32} \mathbf{y}_2 \quad (\text{A.15})$$

being the solution of the system of equations (A.1) obtained by back substitution

$$\mathbf{U}_{33} \mathbf{x}_3 = \mathbf{y}_3 \quad (\text{A.16})$$

$$\mathbf{L}_{22}^T \mathbf{x}_2 = \mathbf{y}_2 - \mathbf{L}_{32}^T \mathbf{x}_3 \quad (\text{A.17})$$

$$\mathbf{L}_{11}^T \mathbf{x}_1 = \mathbf{y}_1 - \mathbf{L}_{21}^T \mathbf{x}_2 - \mathbf{L}_{31}^T \mathbf{x}_3 \quad (\text{A.18})$$

Appendix B. Implementation of the contact lookup table

For computing the contact lookup table, the track and wheelset are assumed to be rigid. The relative motion between them occurs in the $y_t z_t$ plane, being the wheelset allowed to rotate about the longitudinal x_t axis (roll rotation). Furthermore, the contact between the wheel and rail occurs at only one point and no separation is allowed. Under these assumptions, the surface parameters s_r and s_w can be computed as a function of the relative lateral displacement Δy .

Since the accuracy of the contact table depends on the degree of discretization used, the wheel and rail surfaces are discretized by a set of points that reliably represent the profile geometry. Hence, for a given relative lateral displacement of the wheelset, the vertical distances between each point of the wheel and rail surfaces are evaluated. Using this set of vertical distances, the points with maximum absolute value, which belong to the intersection between the wheel and rail

surfaces, are considered to be potential contact points. Since the wheelset is rigid, the potential contact points are in contact only if the following condition is met

$$\left| \Delta z_{\max}^{lft} - \Delta z_{\max}^{rht} \right| < \varepsilon \quad (\text{B.1})$$

where Δz_{\max} is the maximum absolute vertical distance between the wheel and rail in the region where the surfaces intersect each other, and ε is a specified tolerance. The superscripts *lft* and *rht* indicate left and right side of the wheelset, respectively.

If the condition (B.1) is not fulfilled, the wheelset roll rotation ϕ_w has to be iteratively adjusted. According to [34], the number of iterations can be substantially reduced if the roll rotation of the wheelset is adjusted by an angle $\Delta\phi_w$ given by

$$\Delta\phi_w = \frac{\Delta z_{\max}^{lft} - \Delta z_{\max}^{rht}}{y_{\max}^{t,lft} - y_{\max}^{t,rht}} \quad (\text{B.2})$$

where y'_{\max} is the lateral displacement of the points of the wheel with maximum absolute vertical distance to the rail, in the region where the surfaces intersect each other, with respect to the target element coordinate system. The contact search is repeated until the tolerance specified in the condition (B.1) is satisfied.

It is important to emphasize that the contact lookup table is used exclusively to obtain an initial estimate for the solution of the nonlinear equations (21) and to predict if there is a contact jump between the wheel tread and the flange.

References

- [1] Xia H, Guo W, Wu X, Pi YL, Bradford MA. Lateral dynamic interaction analysis of a train–girder–pier system, *Journal of Sound and Vibration* 2008; 318: 927-942. DOI:10.1016/j.jsv.2008.05.002.
- [2] Zhang N, Xia H, Guo W. Vehicle-bridge interaction analysis under high-speed trains, *Journal of Sound and Vibration* 2008; 309: 407-425. DOI:10.1016/j.jsv.2007.07.064.
- [3] Wu YS, Yang YB, Yau JD. Three-dimensional analysis of train-rail-bridge interaction problems, *Vehicle System Dynamics* 2001; 36: 1-35. DOI:10.1076/vesd.36.1.1.3567.

- [4] Zhang N, Xia H, Guo W, De Roeck G. A vehicle-bridge linear interaction model and its validation, *International Journal of Structural Stability and Dynamics* 2010; 10: 335-361. DOI:10.1142/S0219455410003464.
- [5] Antolín P, Goicolea JM, Oliva J, Astiz MA. Nonlinear train-bridge lateral interaction using a simplified wheel-rail contact method within a finite element framework, *Journal of Computational and Nonlinear Dynamics* 2012; 7: art. no. 041014. DOI:10.1115/1.4006736.
- [6] Bozzone E, Pennestrì P, Salvini P. Dynamic analysis of a bogie for hunting detection through a simplified wheel-rail contact model, *Multibody System Dynamics* 2011; 25: 429-460. DOI:10.1007/s11044-010-9233-8.
- [7] Tanabe M, Matsumoto N, Wakui H, Sogabe M, Okuda H, Tanabe Y. A simple and efficient numerical method for dynamic interaction analysis of a high-speed train and railway structure during an earthquake, *Journal of Computational and Nonlinear Dynamics* 2008; 3: DOI:10.1115/1.2960482.
- [8] Falomi S, Malvezzi M, Meli E. Multibody modeling of railway vehicles: Innovative algorithms for the detection of wheel-rail contact points, *Wear* 2010; 271: 453-461. DOI:10.1016/j.wear.2010.10.039.
- [9] Pombo J, Ambrosio J, Silva M. A new wheel-rail contact model for railway dynamics, *Vehicle System Dynamics* 2007; 45: 165-189. DOI:10.1080/00423110600996017.
- [10] Shabana A, Tobaa M, Sugiyama H, Zaazaa KE. On the computer formulations of the wheel/rail contact problem, *Journal of Sound and Vibration* 2005; 40: 169-193. DOI:10.1007/s11071-005-5200-y.
- [11] Zhai W, Wang K, Cai C. Fundamentals of vehicle-track coupled dynamics, *Vehicle System Dynamics* 2009; 47: 1349-1376. DOI:10.1080/00423110802621561.
- [12] Neves SGM, Azevedo AFM, Caçada R. A direct method for analyzing the vertical vehicle-structure interaction, *Engineering Structures* 2012; 34: 414-420. DOI:10.1016/j.engstruct.2011.10.010.
- [13] Neves SGM, Montenegro PA, Azevedo AFM, Caçada R. A direct method for analyzing the nonlinear vehicle-structure interaction, *Engineering Structures* 2014; 69: 83-89. DOI:10.1016/j.engstruct.2014.02.027.
- [14] MATLAB[®]. Release R2011b, The MathWorks Inc., Natick, MA, USA; 2011.
- [15] ANSYS[®]. Academic Research, Release 13.0, ANSYS Inc., Canonsburg, PA, USA; 2010
- [16] Polach O. A fast wheel-rail forces calculation computer code, *Vehicle System Dynamics* 1999; 33: 728-739.
- [17] Bathe KJ. *Finite element procedures*. Prentice-Hall, Upper Saddle River, NJ, USA; 1996.
- [18] Hertz H. Ueber die Berührung fester elastischer Körper [On the contact of elastic solids], *Journal für die reine und angewandte Mathematik* 1882; 92: 156-171.
- [19] Goldsmith W. *Impact: The theory and physical behaviour of colliding solids*. Edward Arnold Ltd., London, UK; 1960.
- [20] Shabana A, Zaazaa KE, Sugiyama H. *Railroad vehicle dynamics: A computational approach*. CRC Press, Boca Raton, USA; 2008.
- [21] Owen DRJ, Hinton E. *Finite Elements in Plasticity: Theory and Practice*. Pineridge Press Limited, Swansea, UK; 1980.
- [22] Kalker JJ. Book of tables for the Hertzian creep-force law, 2nd Mini Conference on Contact Mechanics and Wear of Wheel/Rail Systems, Budapest, Hungary; 1996.
- [23] CONTACT[®]. Release 11.1, VORtech Computing, Delft, the Netherlands; 2011.
- [24] Kalker JJ. The computation of three-dimensional rolling contact with dry friction, *International Journal for Numerical Methods in Engineering* 1979; 14: 1293-1307. DOI:10.1002/nme.1620140904.
- [25] Kalker JJ. On the rolling contact of two elastic bodies in the presence of dry friction. PhD thesis, Delft University of Technology, Delft, The Netherlands; 1967.
- [26] Hughes TJR. *The finite element method: Linear static and dynamic finite element analysis*. Dover Publications, New York, NY, USA; 2000.
- [27] Matsumoto N, Sogabe M, Ichiro S, Manabu I. Outline of design standard for railway structures (displacement limits), *Railway Technical Research Institute Report* 2006; 20: 5-8 [in Japanese].
- [28] Sogabe M, Furukawa A, Shimomura T, Iida T. Displacement limits of structures for high-speed train operation, *Railway Technical Research Institute Report* 2006; 20: 13-18 [in Japanese].

- [29] Railway Technical Research Institute - Testing facilities. http://www.rtri.or.jp/eng/rd/rd_test.html (Accessed 19 Dec 2013).
- [30] Sogabe M, Furukawa A, Shimomura T, Iida T, Matsumoto N, Wakui H. Deflection limits of structures for train speed-up, Quarterly Report of Railway Technical Research Institute 2005; 46: 130-136. DOI:10.2219/rtriqr.46.130.
- [31] Tanabe M, Wakui H, Matsumoto N, Okuda H, Sogabe M, Komiya S. Computational model of a Shinkansen train running on the railway structure and the industrial applications, Journal of Materials Processing Technology 2003; 140: 705-710. DOI:10.1016/S0924-0136(03)00777-5.
- [32] Matsumoto Y. Japanese Railway Technology Today. East Japan Railway Culture Foundation, Tokyo, Japan; 2001.
- [33] Burden RL, Faires JD. Numerical analysis, 6th ed. ITP, Pacific Grove, CA, USA; 1997.
- [34] Li Z. Wheel-rail rolling contact and its application to wear simulation. PhD thesis, Delft University of Technology, Delft, The Netherlands; 2002.